Journal of Oceanography, Vol. 55, pp. 307 to 325. 1999

Winds and Waves in the Yellow and East China Seas: A Comparison of Spaceborne Altimeter Measurements and Model Results

PAUL A. HWANG[1], STEVEN M. BRATOS[2], WILLIAM J. TEAGUE[1], DAVID W. WANG[3], GREGG A. JACOBS[1] and DONALD T. RESIO[2]

[1]*Oceanography Division, Naval Research Laboratory, Stennis Space Center, MS 39529-5004, U.S.A.*
[2]*U.S. Army Engineer Waterways Experiment Station, Vicksburg, MS 39180-6199, U.S.A.*
[3]*Computer Science Corporation, Stennis Space Center, MS 39529-5004, U.S.A.*

(Received 13 July 1998; in revised form 15 October 1998; accepted 17 November 1998)

Wind speed and wave height measured by satellite altimeters represent a good data source to the study of global and regional wind and wave conditions. In this paper, the TOPEX altimeter wind and wave measurements in the Yellow and East China Seas are analyzed. The results provide a glimpse on the statistical properties and the spatial distributions of the regional wind and wave conditions. These data are excellent for use in the validation and verification of numerical simulations on global and regional scales. The altimeter measurements are compared with model output of temporal statistics and spatial distributions. The results show that the model simulations are in good agreement with TOPEX measurements in terms of the local mean and standard deviation of the variables (wave height and wind speed). For the comparison of spatial distributions, the quality of agreement between numerical simulations and altimeter measurements varies significantly from cycle to cycle of altimeter passes. In many cases, trends in the spatial distributions of wave heights and wind speeds between simulations and measurements are opposite. The statistics of biases, rms differences, linear regression coefficients and correlation coefficients are presented. A rather large percentage (~50%) of cases show poor agreement based on a combination of low correlation, large rms difference or bias, and poor regression coefficient. There are indications that wave age is a factor affecting the performance of wave modeling skills. Generally speaking, the error statistics in the wave field is correlated to the corresponding error statistics in the wind field under the condition of active wind-wave generation. The error statistics between the wave field and the wind field become less correlated for large wave ages.

Keywords:
· Wind,
· wave,
· wave age,
· climatology,
· spaceborne altimeter,
· East China Sea,
· Yellow Sea,
· Kuroshio,
· model comparison.

1. Introduction

Remote sensing from space provides a synoptic view of the ocean wind and wave fields. For example, wind speed and significant wave height are standard outputs of spaceborne altimeters such as TOPEX/POSEIDON (hereafter referred to as TOPEX for brevity). Comparisons of the altimeter measured wind speed and wave height with surface buoy data have shown very positive agreement (e.g., Brown *et al.*, 1981; Chelton and Wentz, 1986; Ebuchi and Kawamura, 1994; Freilich and Challenor, 1994; Gower, 1996; Hwang *et al.*, 1998a). For the significant wave height, the bias is on the order of a few centimeters, the rms difference is approximately 0.14 m, the regression coefficient (that is, the slope of the scatter plot when the intercept is forced to zero, representing the proportionality factor between altimeter and buoy data) is between 0.97 to 1.0, and the correlation coefficient is 0.97. For wind speed, the bias is approximately 0.13 m/s, the rms difference is 1.3 m/s, the proportionality factor is between 0.98 to 1.12, and the correlation coefficient is 0.85. These statistics illustrate the high accuracy of wind speeds and wave heights measured by spaceborne altimeters.

With an along-track resolution of 7 km, the spaceborne measurements represent a valuable addition to the study of regional oceanography. The spatial resolution of the spaceborne altimeter in the groundtrack direction is comparable to or better than that of the numerical models used for regional simulations. One of the major issues in the numerical hindcasting and forecasting is the difficulty of validation and verification. While comparisons with point measurements from discrete and sparsely distributed wave buoys provide some degree of statistical confidence, the spatial distribution of the modeled wind and wave fields cannot be easily assessed.

Spaceborne altimeter outputs have been used for model validation, data assimilation and/or evaluation of model performance with different wind products. The number of publications on these topics is quite large (e.g., Janssen *et al*., 1989; Bauer *et al*., 1992; Lionello *et al*., 1992; Romeiser, 1993; Bauer and Staabs, 1998; Sterl *et al*., 1998) and we shall limit the scope of review here. Bauer *et al*. (1992) compare global distribution of wave heights from WAM hindcast with Seasat altimeter output. They found a significant underestimation of wave heights by WAM hindcast for the southern hemisphere. The main reason for the discrepancy is attributed to that the wind stress that drives the wave model is too low. In the study, they also compared the effects of three different wind fields, produced by the Goddard Laboratory for Atmospheres (GLA), the European Centre for Medium-Range Weather Forecasts (ECMWF), and the Jet Propulsion Laboratory (JPL), on the WAM model outputs. One feature in common to the GLA and JPL simulation runs is that WAM overestimate wave heights (as compared to the altimeter measurements) at low sea state and underestimate wave heights at high sea state. The transition occurs at approximately 3 m in the significant wave height. Using the ECMWF winds, the WAM output exceeds the altimeter wave height in all sea states but the general agreement is considerably better than the other two hindcast runs (see figures 8 to 10 of Bauer *et al*., 1992). Similar features are found in the global comparison of WAM output with one-year Geosat wave height data presented in Romeiser (1993). He shows that the agreement between the wave heights of WAM and Geosat is generally good but significant regional and seasonal differences are found. Particularly, the underestimation of WAM wave heights in the southern hemisphere shows significant seasonal variations. The hindcast wave heights are underestimated by about 20% in large parts of the southern hemisphere and the tropical region during May to September. For the rest of the year, the agreement is fairly good. Their results also show that WAM typically overestimates wave heights at low sea state (significant wave height less than 1.5 m approximately). WAM model outputs are also used to perform global calibration of wave height measurements obtained by altimeters of four different satellites (Bauer and Staabs, 1998). Detailed results and discussions presented include the time series and comparison of the monthly means and rms deviations between each altimeter and the WAM model in three geophysical zones (three bands of 40 degrees latitudes each between 60°S to +60°N), and the probability distributions of the global wave heights obtained from the WAM model and all the satellite altimeters investigated.

In the following, we analyze the TOPEX data along two groundtracks in the region of Yellow and East China Seas for the year 1994. The results are used to investigate the regional statistics and spatial distributions of winds and waves. Also presented are the results of a comparison study with the output of the WAM model simulation. Section 2 describes the Yellow and East China Seas data sets and provides background information concerning the numerical modeling and satellite groundtracks in the comparison region. Section 3 presents the results and comparison of temporal averages. Statistics such as bias (B), rms difference (Δ), regression coefficients (c and c_y, to be further discussed later) and correlation coefficient (R) are calculated. Since altimeter remote sensing provides spatial coverage of the wind and wave fields along transects, we will explore the use of such information for the validation of the spatial distribution of wave heights from model output. The results are presented in Section 4. The conclusions and summary are presented in the last section of the paper.

2. Yellow and East China Seas Data Sets

2.1 A brief description of the region

The Yellow and East China Seas are on a large and shallow continental shelf, with depths less than 100 m in most of the region. The major current system in the region is the Kuroshio, which enters the Yellow and East China Seas just southeast of Taiwan and exits just southwest of Japan. The main axis of the Kuroshio in this region is usually outside of the 200 m contour line. The Kuroshio may intrude onto the shelf through two major regions. The first is through the Taiwan Strait during the winter months when the Taiwan Warm Current is weak (Chuang and Liang, 1994). The second source is the branching of the Tsushima Current from the Kuroshio (Lie and Cho, 1994) and the subsequent intrusion of the Yellow Sea Warm Current northward into the Yellow Sea (Hsueh, 1988; Hsueh *et al*., 1993). One of the driving forces of the Yellow Sea Warm Current and the flux of open ocean properties onto the continental shelf is the northerly wind bursts during the winter season. Due to the shallow water depth, the wind events are capable of creating large sea level changes, which produce horizontal pressure gradients that drive the subsurface currents (Hsueh, 1988).

The wind system is influenced by the monsoon wind pattern of Asia. In the winter, the Mongolian high-pressure system dominates the geostrophic winds and forms an anticyclonic gyre in the region. The primary wind direction in the winter months is northwesterly in the north, and northerly or northeasterly in the East China Sea. During the summer, the Indian Ocean low-pressure system dominates, creating a cyclonic gyre in the region. The wind direction is southerly to southeasterly in the whole region. During the transitional season between the two dominant weather systems, the winds fluctuate (Wang and Aubrey, 1987). The wave system is significantly affected by the wind system.

2.2 WAM model output

The WAM model (Cycle 4) (WAMDI Group, 1988;

Janssen, 1991) was recently applied to the Yellow and East China Seas to hindcast the wave climatology for 1994. The wave hindcast setup consisted of a global 1° Lat/Lon grid to generate input wave boundary conditions and a regional 0.25° Lat/Lon grid for the domain that includes the Yellow Sea, East China Sea, and the Sea of Japan.

A global wind product (Wobus and Kalnay, 1995) from the National Centers for Environmental Prediction (NCEP, formerly the National Meteorological Center) was used to drive the global and regional wave model grids. The NCEP winds, which are provided at approximately 0.94° Lat/Lon resolution, were bilinearly interpolated to a 1° resolution for the global hindcast and a 0.25° resolution for the regional hindcast. The global hindcast was run with a temporal resolution of 6 hours, which is the resolution provided by NCEP. The NCEP winds were linearly interpolated to a 3 hour resolution for the regional hindcast. One of the standard WAM output files includes the significant wave height (SWH), H_s, friction velocity u^*, and drag coefficient C_D at every grid point. The model wind speed at a 10 m elevation is computed by $U_{10} = u^* C_D^{-1/2}$. The wave height, wave direction, wave period (peak and average), wind speed and wind direction of the model outputs are extracted along two TOPEX groundtracks for comparison. A more detailed description of WAM and NCEP models is given in Appendix A.

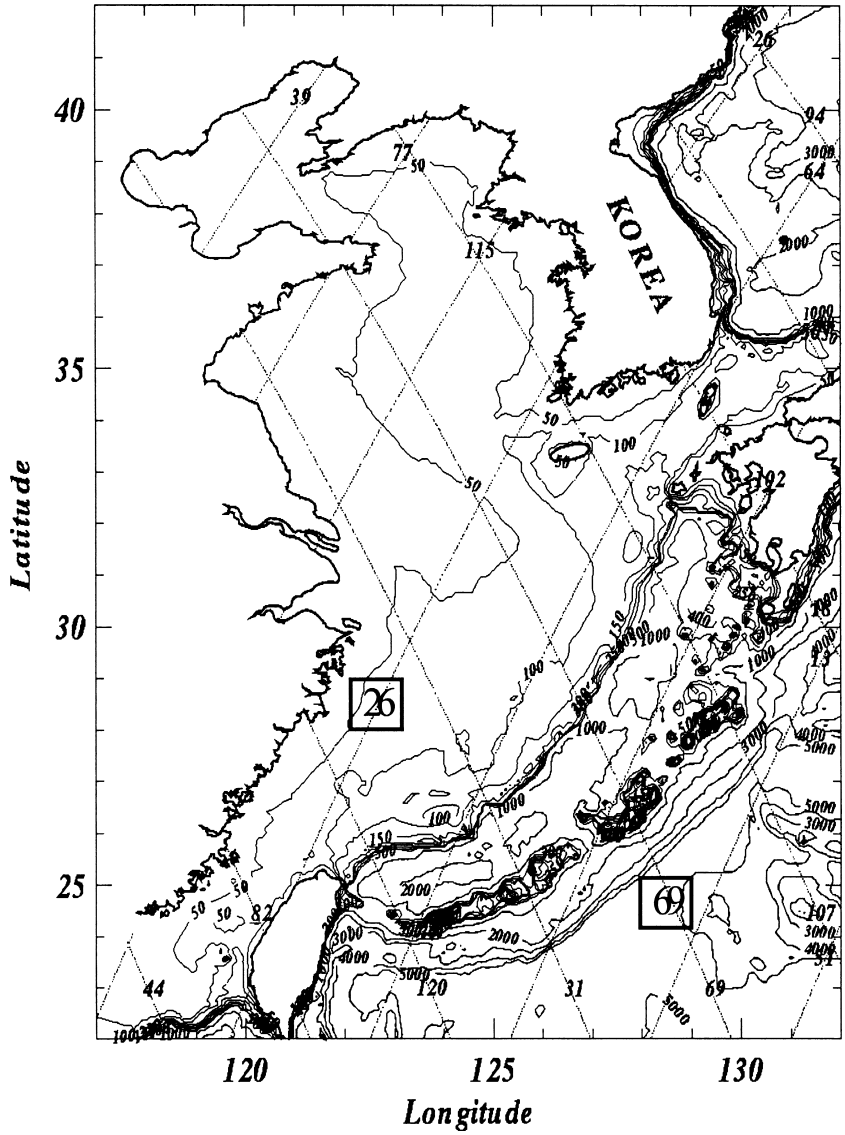

Fig. 1. A map of the Yellow and East China Seas region for this comparison study. TOPEX groundtracks are shown in dotted curves. Tracks 69 (from NW to SE going through the axis of the region) and 26 (from SW to NE across the Yellow and East China Seas entrance) are used for comparison with WAM model simulation for the year 1994.

2.3 Combined TOPEX and WAM data set

The TOPEX groundtracks in the Yellow and East China Seas region are shown in Fig. 1. The bathymetry of the region, based on ETOPO 5 (NOAA, 1986), is contoured in Fig. 1 also. Of the 17 groundtracks falling within the region shown in Fig. 1, two are selected for this study. The first groundtrack is number 69, a descending track that runs along the central axis of the region. The second groundtrack is number 26, which is an ascending track cutting across the East China Sea and the southeast corner of the Yellow Sea. Water depths along these two groundtracks are mostly greater than 50 m, except near Taiwan and Korea coasts (Track 26), Ryukyu Islands and Shandong Peninsula (Track 69), and the region of marine deposit from old Yellow River discharge extending to the central and southern parts of the Yellow Sea (Fig. 1).

The extraction of the model output consists of interpolation of the model parameters to the satellite groundtrack coordinates using two subroutines (*surface* and *grdtrack*) within the GMT-System (Generic Mapping Tools) (Wessel and Smith, 1991). These subroutines create a 2-D binary grid file using an adjustable tension continuous curvature algorithm, and then sample the 2-D binary grid file along groundtracks 26 and 69 using bicubic interpolation (Smith and Wessel, 1990). The numerical output and altimeter data are then merged together by linear interpolation to a uniform spacing of 0.05 degree using the latitude coordinate as reference. The spacing between neighboring data points in the merged data set is between 6.0 to 6.3 km along the groundtrack. The distance between the model data position and the interpolated altimeter footprint is between 0.4 to 0.6 km.

3. Temporal Average

Over the one-year (1994) model run, 32 cycles are extracted for each groundtrack. The TOPEX/POSEIDON mission splits time between the NASA Ku and C-band radars (90%) and the CNES (POSEIDON) solid state altimeter (10%). The 4 missing cycles occur at Julian days 63, 172, 311 and 361 for groundtrack 26, and days 76, 176, 315 and 324 for groundtrack 69. The time differences between the model output and TOPEX measurement are distributed approximately evenly between 0 to 1.5 hours. In the merged data set, the data density is 20 points per degree per satellite cycle. The number of data points used in the averaging shown below can be computed easily. For example, the data population for the seasonal (quarterly) average (8 cycles) over a latitude span of 3 degrees is 480 (that is, $8 \times 3 \times 20$), and the annual average (32 cycles) over a 9-degree span is 5760. These data are not fully independent as they have been

Table 1. Comparison of mean and standard deviation of WAM and TOPEX average data.

A. Annual average over a region								
Latitude Range	Wave Height				Wind Speed			
	$\langle H_s \rangle$ (m)		$\sigma_H/\langle H_s \rangle$		$\langle U_{10} \rangle$ (m/s)		$\sigma_U/\langle U_{10} \rangle$	
	TOPEX	WAM	TOPEX	WAM	TOPEX	WAM	TOPEX	WAM
(a) Track 69								
D9 (27.5, 36.5)	1.45	1.55	0.58	0.54	6.66	6.94	0.51	0.49
S3 (27.5, 30.5)	1.70	1.85	0.45	0.37	7.19	6.99	0.46	0.51
M3 (30.5, 33.5)	1.49	1.53	0.65	0.55	6.66	6.97	0.52	0.45
N3 (33.5, 36.5)	1.16	1.21	0.58	0.74	6.15	6.84	0.53	0.50
(b) Track 26								
D9 (25.5, 34.5)	1.65	1.81	0.56	0.56	7.02	7.78	0.49	0.42
S3 (25.5, 28.5)	1.82	1.98	0.54	0.52	7.49	7.75	0.48	0.46
M3 (28.5, 31.5)	1.63	1.81	0.47	053	6.50	7.76	0.49	0.43
N3 (31.5, 34.5)	1.51	1.54	0.59	0.61	7.07	7.87	0.50	0.38

interpolated from a coarser numerical grid of 0.25° (approximately 25 km) and altimeter spacing of 7 km. For the purpose of estimating the degrees of freedom, or equivalently the confidence interval, those population numbers should be divided by a factor of 4.

3.1 Annual average

We first study the wave and wind statistics derived from TOPEX measurements and the numerical output of WAM and NCEP. The annual averages along the two groundtracks are listed in Table 1A. An example of the statistical distributions of winds and waves in four different regions (defined below) are shown in Fig. 2 (top half), in which the histograms of wind speeds and wave heights along groundtrack 69 are displayed. These four regions are designated as D9, S3, M3 and N3 for 9 degrees (latitude), southern 3 degrees, middle 3 degrees and northern 3 degrees along the two groundtracks. The limiting latitudes are tabulated in the first column of Table 1A.

As shown in the figure and the tabulated statistics, the average properties of wind speeds and wave heights between the numerical simulation and remote sensing measurements are in good agreement, within 10 percent in most cases for both the mean and standard deviation of these average quantities. Both data sets also show that the average wave height decreases northward. Along the central axis of Yellow and East China Seas (track 69) the 3-degree average wave height is reduced from 1.70 m at 29°, to 1.49 m at 32° and 1.16 m at 35° based on TOPEX measurements. The average wave height along groundtrack 26 shows a similar trend of decreasing wave height from south to north, with 1.82 m at 27°, 1.63 m at 30° and 1.51 m at 33°. The gradient of the wave height along groundtrack 69 is significantly larger than that along groundtrack 26. Hwang and Teague (1998) and Hwang *et al*. (1998b) have processed the full 17 groundtracks of data to construct the wind and wave climatologies of the region. They found that the wind and wave distributions in the region are significantly modified by the Kuroshio, which runs in the southwest to northeast orientation. As a result, the gradient of the wave height distribution is mainly in the northwest to southeast orientation.

Wave heights for WAM hindcast are slightly higher than the TOPEX data. For the three regions (S3, M3 and N3) along groundtrack 69, the differences are 9%, 3% and 4%, respectively. Along groundtrack 26, the model output again overpredicts the wave height by 9%, 11% and 2%, respectively.

The distribution of the average wave heights within a given segment along groundtrack can be measured in terms

Table 1. (continued).

B. Seasonal average along a groundtrack

Day Range	Wave Height				Wind Speed			
	$\langle H_s \rangle$ (m)		$\sigma_H/\langle H_s \rangle$		$\langle U_{10} \rangle$ (m/s)		$\sigma_U/\langle U_{10} \rangle$	
	TOPEX	WAM	TOPEX	WAM	TOPEX	WAM	TOPEX	WAM
(a) Track 69								
Q1 (1, 90)	1.63	1.76	0.48	0.56	7.60	8.10	0.41	0.44
Q2 (91, 180)	0.96	1.07	0.40	0.36	4.50	5.17	0.57	0.38
Q3 (181, 270)	1.46	1.67	0.69	0.55	6.47	6.74	0.55	0.51
Q4 (271, 360)	1.69	1.67	0.50	0.50	7.85	7.76	0.38	0.45
(b) Track 26								
Q1 (1, 90)	1.69	1.59	0.42	0.40	7.51	7.42	0.43	0.36
Q2 (91, 180)	1.10	1.31	0.28	0.31	4.78	6.50	0.47	0.35
Q3 (181, 270)	1.84	2.14	0.69	0.72	7.06	7.21	0.64	0.63
Q4 (271, 360)	1.90	2.14	0.43	0.36	8.33	9.76	0.29	0.23

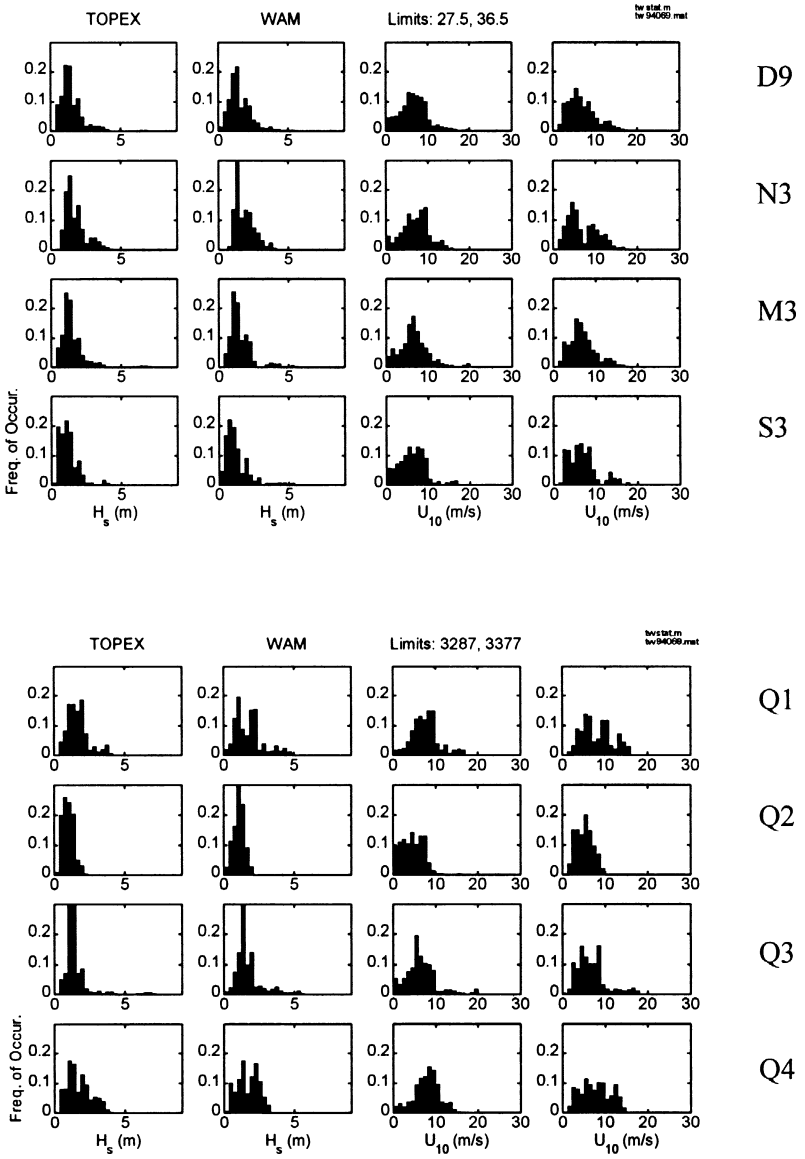

Fig. 2. Histograms of wave heights and wind speeds from TOPEX measurements and WAM output along groundtrack 69. The plots are arranged as H_S (TOPEX), H_S (WAM), U_{10} (TOPEX) and U_{10} (WAM) in the first to the fourth column. The upper four rows of the plots are annual data within 9° (D9), southern 3° (S3), middle 3° (M3), and northern 3° (N3) latitude, respectively. The lower four rows are the histograms of the wind and wave parameters in the 9° latitude, and over the first to the fourth 90-day period of 1994 data sets.

of the standard deviation (Table 1A). In the along-axis direction (groundtrack 69), the dimensionless standard deviations (normalized by the mean) are 0.45, 0.65 and 0.58 from south to north based on the TOPEX data, and 0.37, 0.55, and 0.74 based on the WAM output. The standard deviations between WAM and TOPEX along groundtrack 26 are in much better agreement (TOPEX: 0.52, 0.53, 0.61, WAM: 0.54, 0.47, 0.69). In general, the annual average predicted by the WAM model agrees very well with the TOPEX measurement. In cases with discrepancies, the disagreement in wave height appears to correlate with disagreement in wind speed or wind stress used to drive the model. As shown in Table 1A, the average wind speed used in WAM is in general higher than the TOPEX observation. Except for one case (groundtrack 69, S3), the average wind used in WAM is 4 to 19% higher than the corresponding TOPEX measurement.

3.2 Seasonal variation

The statistics of seasonal (quarterly) average wave heights and wind speeds from TOPEX and WAM are listed in Table 1B. The histograms of wave heights and wind

speeds of the four quarters are shown in Fig. 2 (lower half). These statistics are based on the data along the full 9-degree groundtrack discussed above. The statistics over a smaller or larger distance can be generated also. Two of the notable features of the seasonal average are (1) the lower average occurs in the second quarter, and (2) the largest variation as represented by the standard deviation occurs in the third quarter (Table 1B). These features are consistent with the monsoon climate of the region, with predominantly northwesterly to northerly winds in the winter, and southwesterly to southeasterly winds in the summer. In the transition seasons, the winds fluctuate between the two dominant weather systems (e.g., Wang and Aubery, 1987). The wind and wave properties are further complicated by the typhoons, which generally occur from July to October, and explain the large variation (standard deviation) of the seasonal statistics during the third quarter.

The agreement of these seasonal mean properties derived from WAM outputs and TOPEX measurements is generally good, the ratios of averages (WAM/TOPEX) range between 0.94 to 1.19. The agreement in the statistics of standard deviations is also similar to that of the seasonal means. The larger difference in the seasonal means (WAM higher by up to 19%; 1.31/1.10 = 1.19, Track 26, Q2, Table 1B) is correlated to, but considerably lower than, the wind conditions used in driving the wave model. The maximum difference of the seasonal average wind speeds is 36% (6.50/4.78 = 1.36). This observation is also applicable to the annual means, where the maximum wave difference is 11% (1.81/1.63 = 1.11; Track 26, M3, Table 1A), and the maximum wind difference is 19% (7.76/6.50 = 1.19).

3.3 Correlation statistics

In the last two subsections, statistics are computed from TOPEX or WAM separately. In this subsection, the statistics correlating WAM and TOPEX data are presented. The annual data populations of TOPEX and WAM are taken from a given segment along the groundtrack. The length of the groundtrack varies from less than 0.25 degree to 9 degrees in latitude. In this computation, TOPEX and WAM are treated as two sets of "wave probes" with a footprint of 5 km. The "time series" from the subsets (averaged over a segment ranging from 0.25 to 9 degrees latitude) are compared. The statistical parameters computed include the bias (B), rms difference (Δ), linear regression coefficients (c_y and c), and correlation coefficient (R). The coefficient c is calculated by minimizing the orthogonal distances of the data points to the linear regression curve. The coefficient c_y is calculated by minimizing the vertical distances between data points and the linear regression curve. The formulae for the coefficients are given in Bauer *et al*. (1992) and Hwang *et al*. (1998a).

Table 2 shows an example of the correlation statistics computed from the annual data populations within 9 degrees

Table 2. Statistical coefficients of WAM and TOPEX correlations.

	Wave Height, H_s					Wind Speed, U_{10}				
Latitude Limit	c_y	c	B (m)	Δ (m)	R	c_y	c	B (m/s)	Δ (m/s)	R
(a) Track 26										
D9 (25.5, 34.5)	1.06	1.07	0.13	0.33	0.93	1.10	1.13	1.07	1.92	0.83
S3 (25.5, 28.5)	1.07	1.09	0.17	0.43	0.92	1.02	1.04	0.37	1.73	0.87
M3 (28.5, 31.5)	1.07	1.09	0.15	0.41	0.91	1.16	1.21	1.60	2.56	0.78
N3 (31.5, 34.5)	1.03	1.06	0.06	0.41	0.90	1.09	1.13	1.20	2.52	0.75
(b) Track 69										
D9 (27.5, 36.5)	1.06	1.08	0.08	0.28	0.93	1.06	1.08	0.57	1.33	0.91
S3 (27.5, 30.5)	1.05	1.08	0.18	0.42	0.86	0.98	1.01	0.06	1.70	0.87
M3 (30.5, 33.5)	0.97	0.99	0.04	0.35	0.93	1.00	1.04	0.63	1.97	0.86
N3 (33.5, 36.5)	1.03	1.10	0.02	0.46	0.83	1.07	1.13	1.01	2.32	0.78

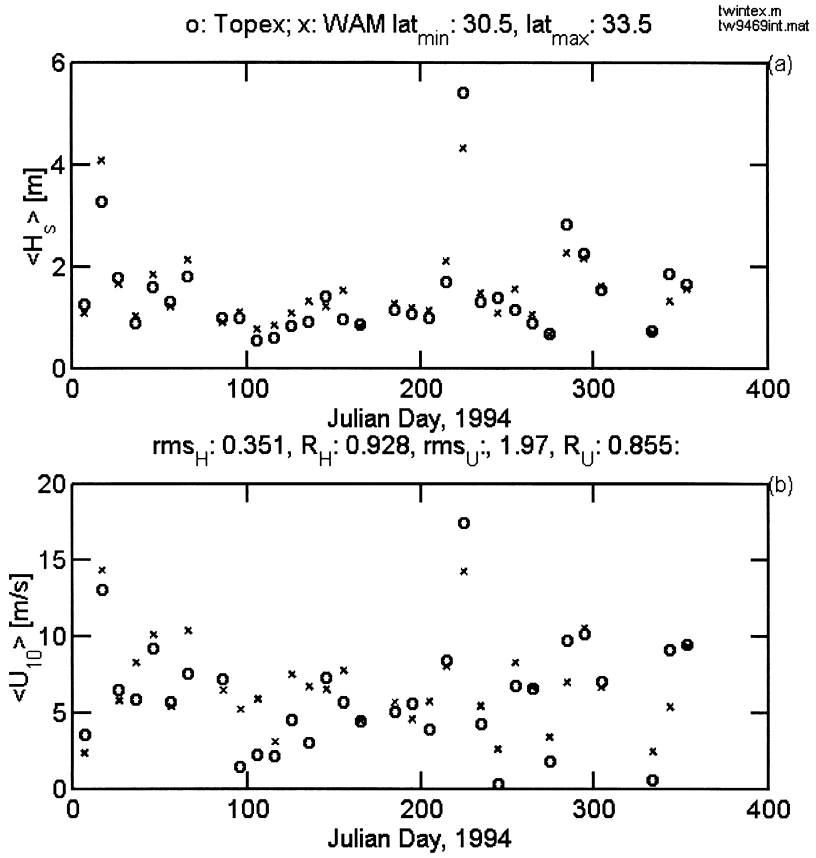

Fig. 3. (a) Mean wave height, and (b) wind speed averaged along groundtrack segments of various distances. The example shown is for the 3-degree average, M3 of groundtrack 69 from 30.5 to 33.5°N (○: TOPEX, ×: WAM).

(D9) and 3 degrees (N3, M3, and S3) latitude. For the wave height, the regression coefficients (proportional factors) c and c_y are predominately larger than unity, indicating that WAM simulated wave heights are higher than TOPEX wave measurements. This is consistent with the averages shown in Table 1. The biases (WAM-TOPEX) in all cases are greater than zero, ranging from 0.02 to 0.18 m. The rms difference for the 9-degree average is approximately 0.3 m, with a correlation coefficient of 0.93 for both groundtracks. The rms difference increases to approximately 0.4 m when the averaging distance decreases and the correlation coefficient also decreases slightly.

For the wind speed, the regression coefficients are again greater than one in most of the cases, indicating that the wind speed used as the model input is larger than the TOPEX wind measurement. For the 9-degree average, the wind speed biases high, with a range from 0.4 to 1.6 m/s. The rms difference is 1.92 m/s for groundtrack 26 and 1.33 m/s for groundtrack 69, with the correlation coefficients of 0.83 and 0.91, respectively. The statistics for the 3-degree (southern, middle, and northern) results degrade somewhat.

In additional to the statistics based on the annual data within the latitude segments (ranging from 0.25 to 9 degrees latitude), the mean wave height and wind speed averaged within the given segment for each cycle are calculated. This is the equivalent of the TOPEX and WAM time series smoothed over the specified segment range. Figure 3 shows an example of the 3-degree average (M3, groundtrack 69). The temporal sampling is very coarse (9.9 days interval) and the seasonal fluctuation is barely discernable. During this year (1994), the winds and waves are mild in the spring time. There are a few burst events in the summer and winter seasons. These time series of wind speed and wave height from WAM and TOPEX are in very good agreement.

4. Spatial Distribution

One of the most significant advantages of remote sensing measurements is the ability to provide a quasi-instantaneous measurement of the spatial distribution of wave heights and wind speeds. For example, the 9° latitude transects of groundtracks 26 and 69 are completed in 168 and 190 s, respectively. The high spatial density (every 7 km in the original TOPEX output) of these quasi-simultaneous measurements is unique for studying the spatial distributions of winds and waves. The data are also excellent for the purpose of comparing spatial patterns of model simulations.

Similar to the analysis presented in the last section, the separate patterns of TOPEX and WAM are compared first in Subsection 4.1. The correlation statistics of the TOPEX and WAM patterns are then calculated in Subsection 4.2.

4.1 Seasonal and annual characteristics

The cycle-by-cycle distributions of wave heights (top half) and wind speeds (bottom half) derived from WAM and TOPEX are shown in Fig. 4 for the full 32 cycles along groundtrack 69. The latitude range shown is 9 degrees (27.5°N to 36.5°N). In general, the TOPEX data display more fine structures in the distribution because the results were obtained from 7-km original resolution. In contrast, the WAM outputs are interpolated from 0.25 degree (approximately 25 km) resolution and are apparently more smoothed. The level of agreement of these TOPEX and WAM spatial patterns varies significantly from cycle to cycle. There is a large fraction of cases with poor agreement either in magnitude, trend (phase), or both. The correlation statistics of individual cycles will be presented in the next subsection.

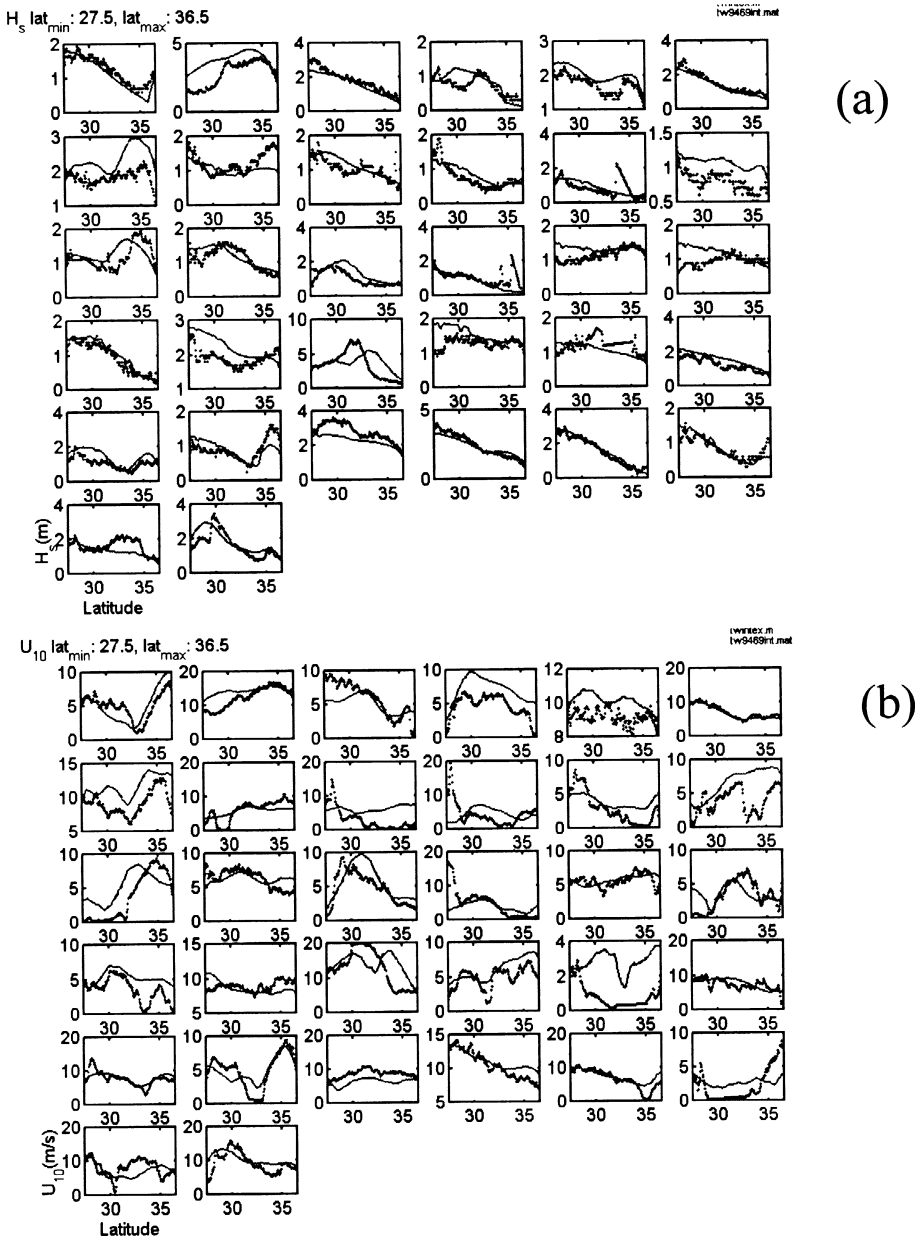

Fig. 4. Cycle-by-cycle comparison of the (a) wave height, and (b) wind speed from TOPEX (dot) and WAM (solid curve) for 32 cycles along TOPEX groundtrack 69.

Here we present these along groundtrack patterns based on the seasonal and annual ensemble averages.

Figure 5 shows the quarterly and annual averages of the wind speed and wave height distributions along groundtrack 69. The measurements of wave heights and wind speeds from TOPEX are shown on the top row, and those from WAM are shown in the bottom row. The equivalent results for groundtrack 26 are shown in Fig. 6. There are several distinct features of these seasonal and annual variations of winds and waves based on the TOPEX measurement. The annual average shows a general decreasing trend of wave height toward north, as was shown in the last section (Subsection 3.1) with a much coarser 3-degree average (Table 1A). The largest gradient of wave heights along groundtrack occurs in the fourth quarter, at the height of the winter monsoon. The lowest wind and wave conditions occur in the second quarter. Along groundtrack 69, a local maximum near 28.2°N appears in 3 quarters (Q1, Q2, and Q4) in the distributions of wave heights, and in all 4 quarters in wind speeds. This local enhancement is not found along groundtrack 26. A more extensive analysis of the TOPEX data (using measurements from all groundtracks) indicates that the local enhancement is attributed to the Kuroshio modification of winds and waves (Hwang and Teague, 1998; Hwang *et al.*, 1998b).

The seasonal variations described in the last paragraph are identifiable in the WAM result also. The fine features between the TOPEX and WAM outputs, however, are significantly different on several occasions. For easier comparison, the seasonal and annual variations are replotted in Figs. 7 (groundtrack 69) and 8 (groundtrack 26), with TOPEX and WAM results plotting over each other in the same blocks. In general, the agreement in the significant wave height is very good in winter months even though wind speeds may show large discrepancies (e.g., Q4 of Track 26, Fig. 8). The wave height comparison in the summer/fall months (Q2 and Q3) is noticeably worse for both groundtracks. Although this may be partially attributed to the poorer wind speed agreement, it is not unusual to find cases with bad wind speed agreement yet very good wave height comparison (e.g., Q2 of Track 26 near 30°N, Q2 of Track 69 near 28 and 33°N). There are also many cases with good agreement in the wind speed yet bad agreement in the wave height comparison (e.g., Q3 of Track 26 near 28 and 30°N, Q2 of Track 69 near 30°N, and Q3 of Track 69 near 28.5°N and 31.5°N). The mismatch of regions of good agreement in the wind speed and wave height is also observed in the annual average (Y94) shown in Figs. 7 and 8.

The observation of the seasonal dependence of data agreement may imply that the WAM model performs much

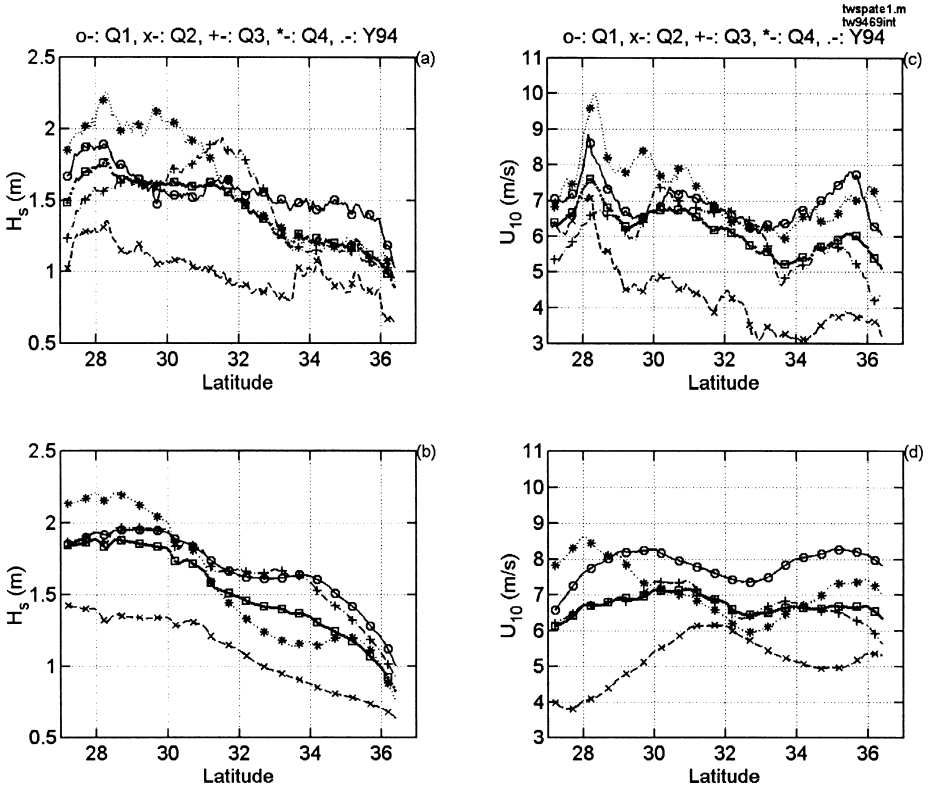

Fig. 5. The spatial distributions of quarterly and annual averages (along groundtrack 69) of wave heights (a) TOPEX, (b) WAM; and wind speed (c) TOPEX, and (d) WAM. (○: quarter 1, ×: quarter 2, +: quarter 3, *: quarter 4, •: annual average).

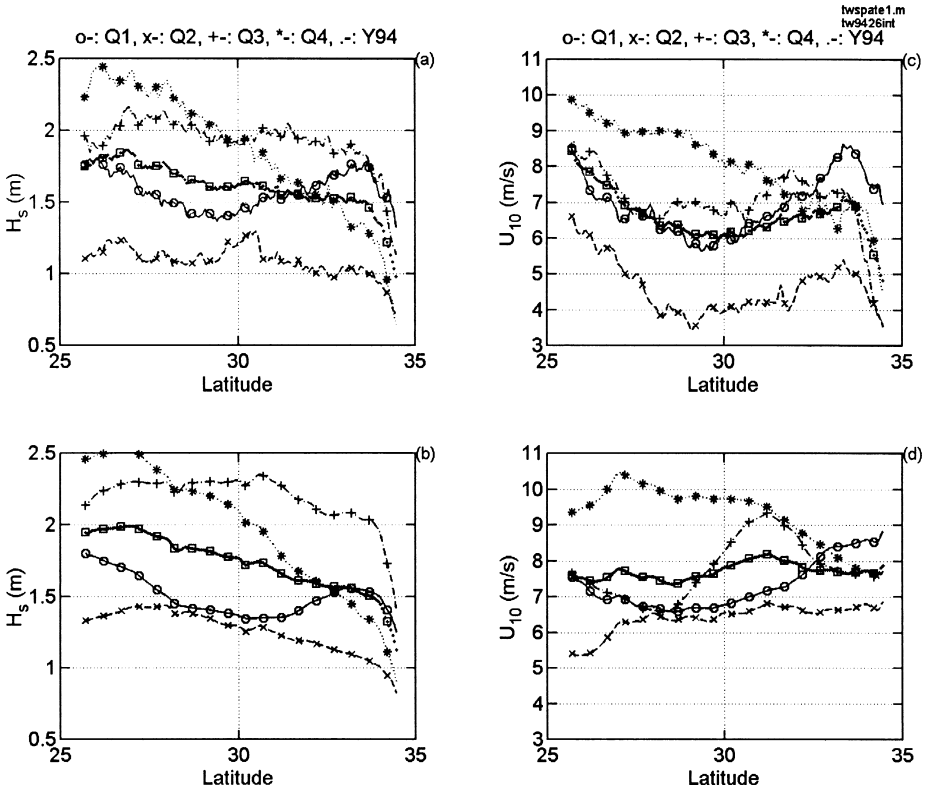

Fig. 6. Same as Fig. 5 but along groundtrack 26.

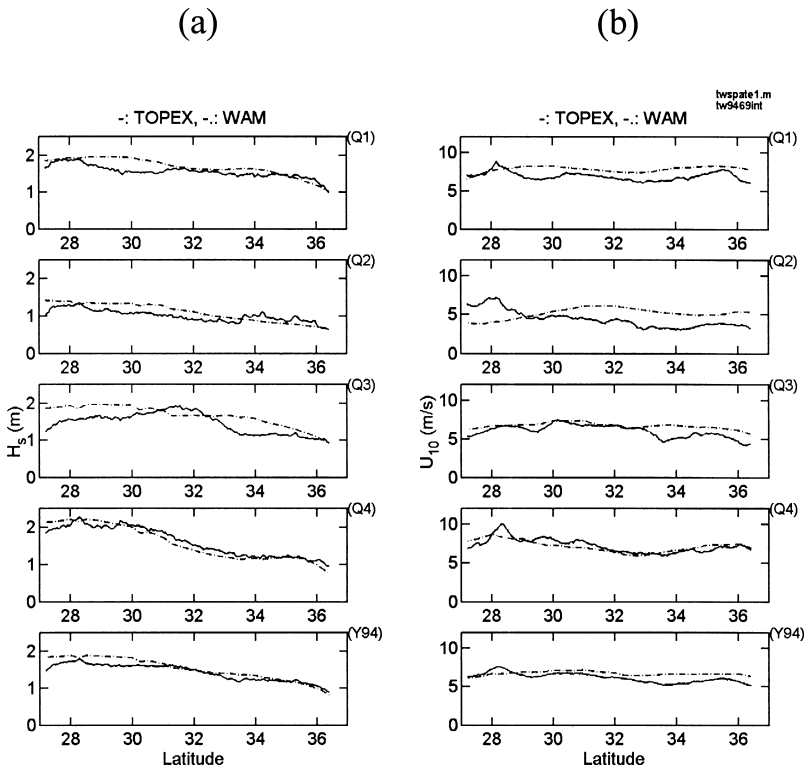

Fig. 7. The spatial distribution of the quarterly averages (Q1 to Q4) and annual average (Y94) of (a) wind speeds, and (b) wave heights along groundtrack 69. Solid lines are TOPEX measurement, and dashed-and-dotted lines are WAM outputs.

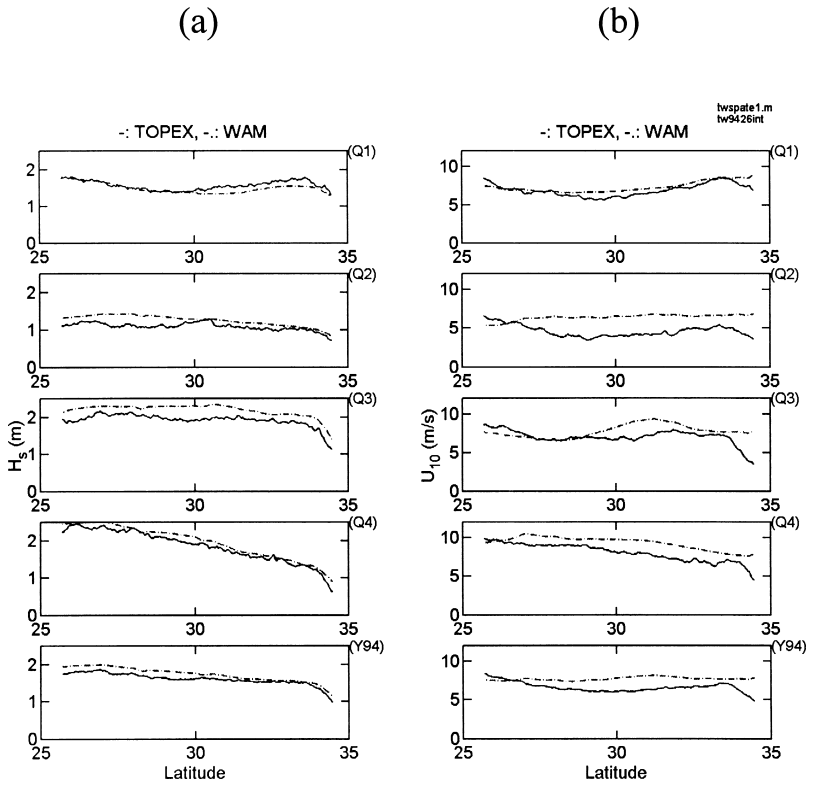

Fig. 8. Same as Fig. 7 but along groundtrack 26.

better in cases of active wind generation, such as during the winter months in the Yellow and East China Seas when the dominant wind is from the north. In the summer months, the performance of the model deteriorates due to a combination of the presence of swell from the south and southeast, and much lower wind speeds during the summer season. These comparisons underline the rather difficult task for numerical simulations to produce accurate spatial distributions of wind and wave properties.

4.2 Correlation statistics

The track-by-track comparison can be further quantified through the analysis of correlation statistics such as bias, rms difference, regression coefficient and correlation coefficient. For the along-axis groundtrack (69) shown earlier in Fig. 4, the WAM wave height output tends to bias high in the first six to nine months of the year and the bias trend reverses toward the winter months (Fig. 9(a)). The bias trend of groundtrack 26 is slightly different, predominantly negative in the first four months, and positive the rest of the year (Fig. 9(b)). While there are apparent similarities in the wave bias and wind bias, the data scatter is large. In dimensionless form, the wave and wind bias can also be normalized by the mean wave height and wind speed, respectively. The average of the normalized wave height bias, $B(H_s)/<H_s>$, is 0.08 for groundtrack 69 and 0.09 for groundtrack 26. For the wind speed bias, $B(U_{10})/<U_{10}>$, the corresponding mean values are much larger, 0.57 and 0.39 for groundtracks 69 and 26, respectively. The cycle-by-cycle scatter index, defined as the normalized rms differences of wave heights, $\Delta(H_s)/<H_s>$, and wind speeds, $\Delta(U_{10})/<U_{10}>$, are plotted in Figs. 9(c) and 9(d) for groundtracks 69 and 26 respectively. The scatter index of wave heights is mostly less than 0.5, with an average value of 0.24 for groundtrack 69 and 0.27 for groundtrack 26. For wind speeds, the average scatter index is 0.77 for groundtrack 69, and 0.55 for groundtrack 26.

The linear regression coefficients (c) for groundtracks 69 and 26 are shown in Figs. 9(e) and 9(f). As can be seen from the plots, there are only a small number of cases with c values close to one. The WAM output tends to over estimate the wave height, especially in the summer months. Many of the wave height over-estimations can be associated with over-estimation of wind speeds used as the input to the wave model. Exceptions are found in very low wind conditions, where the wave heights are mainly dominated by swell components that are unrelated to the local wind condition.

The correlation coefficients between WAM and TOPEX data show the largest variation (Figs. 9(g) and 9(h) for groundtracks 69 and 26, respectively) compared to the other statistical parameters. For the along-axis groundtrack (69),

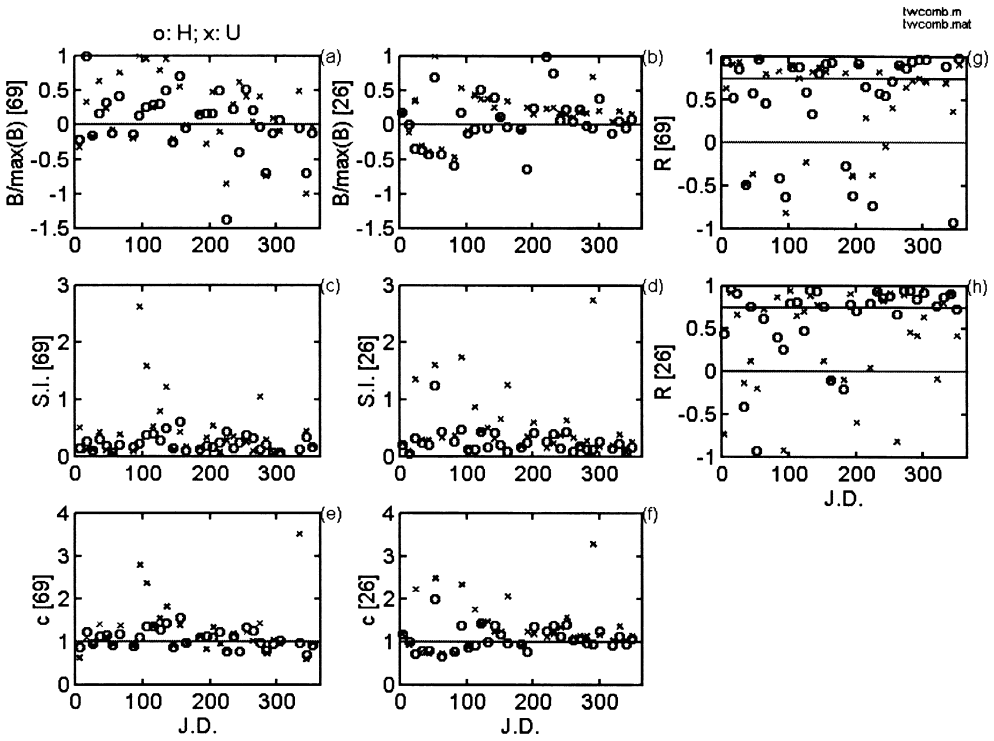

Fig. 9. Statistics comparing spatial distributions of WAM output with TOPEX measurements using M3 averages. Shown here are bias normalized by the maximum for (a) groundtrack 69, and (b) groundtrack 26; rms difference normalized by the mean wave height or mean wind speed for (c) groundtrack 69 and (d) groundtrack 26; regression coefficient for (e) groundtrack 69, and (f) groundtrack 26; and correlation coefficient for (g) groundtrack 69, and (h) groundtrack 26 (○: wave height, ×: wind speed).

7 out of 32 cycles show negative correlation coefficient, which indicates an opposite trend in the wave height distribution along the altimeter groundtrack obtained from WAM modeling as compared to the altimeter measurements. In addition to the cases of negative correlation, 9 more cycles have correlation coefficients less than 0.75. So altogether one half of the cases examined for groundtrack 69 show poor correlation of WAM output with altimeter measurements. Similar to the wave correlation statistics, for the wind speed there are 7 cycles of negative correlations and 9 additional cases of low correlation coefficients. While many cases of poor correlation in wind speeds correspond to those of poor correlation in wave heights, there are mismatches that show good wave correlation but poor wind correlation and vise versa. The cycle-by-cycle statistics of groundtrack 26 are not very different from those of groundtrack 69. For the wave height, there are 4 cases of negative correlation coefficients and 8 cases with $0 < R < 0.75$. For the wind speed, there are 9 negative correlations and 10 cases with $0 < R < 0.75$.

The above conclusions are based on analyzing 32 cycles of 2 groundtracks over a 3-degree latitude region of the satellite groundtracks. Taking a different region along the groundtracks and different time periods for comparison, the statistics will be slightly different from the above results. In all of the statistics discussed above, WAM outputs and TOPEX measurements are in good agreement in about half of the cases. Also, the quality and the scatter of the computed correlation statistics are generally poorer in wind speeds than in wave heights. This suggests that the wave model is relatively more robust and that errors in wind input constitute only partially to the simulation disagreement in wave properties.

4.3 Wave age factor

Several researchers have suggested improvements to WAM (Tolman 1992; Lin and Huang 1996; Bender 1996). Bratos (1997) compares deepwater WAM results to National Data Buoy Center (NDBC) wave measurements along the US Atlantic coast using high quality winds (Cardone, 1992) for five extratropical storms which include a variety of conditions ranging from extreme events to more moderate and variable events. One persistent tendency found in the WAM results is a low bias in the significant wave height. Figure 10(a) shows the relationship between wind speed bias and wave height bias for all buoy locations and storm events considered. For a well behaved model the wave height bias should correspond to the wind speed bias. The plot shows a tendency for WAM wave height to be biased low (0.0 m to –0.5 m) when the wind speed is biased high

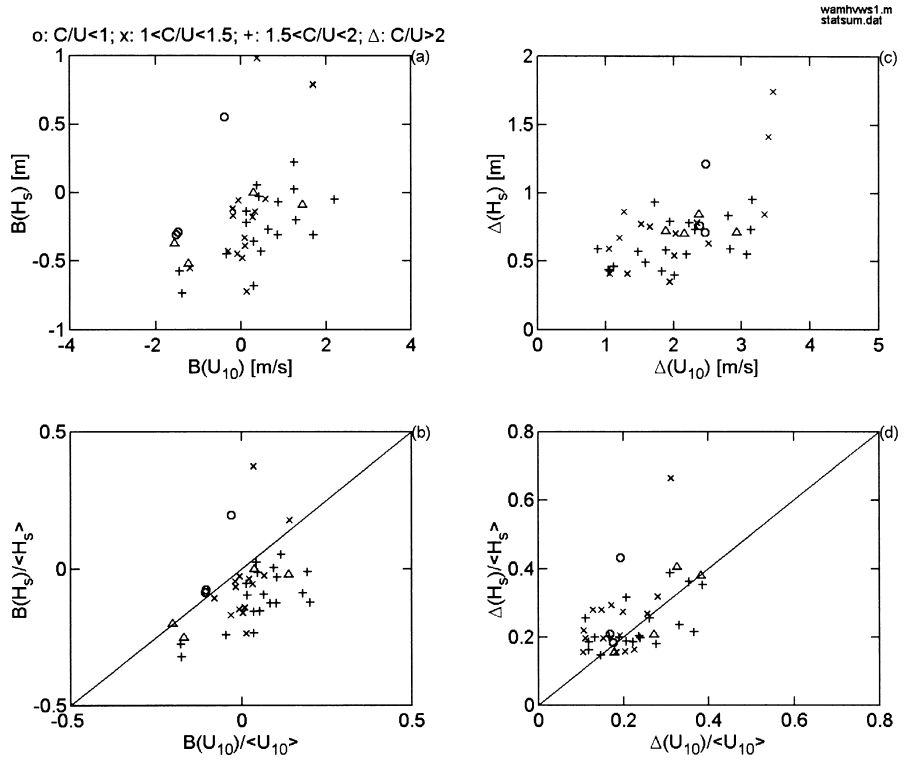

Fig. 10. Scatter plots showing the correlation of (a) bias, and (b) rms difference of wave height with respect to the corresponding quantities of wind speed. The normalized bias and rms difference are shown in (c) and (d), respectively. The data are from the comparison of a WAM simulation and buoy measurements of five storm events in the Atlantic region (Bratos, 1997): Different plotting symbols are used for different ranges of the wave age parameter C/U_{10}: ○: $C/U_{10} \le 1$, ×: $1 < C/U_{10} \le 1.5$, +: $1.5 < C/U_{10} \le 2$, △: $2 < C/U_{10} \le 2.5$, ▽: $2.5 < C/U_{10}$.

(0.0 m/s to 1.75 m/s). The normalized bias (scaled by the mean value of wind speeds or wave heights) is plotted in Fig. 10(b). In a similar fashion, the rms difference in wave heights and wind speeds is shown in Figs. 10(c) and 10(d). The comparison of the wave height parameter from WAM simulations in the Atlantic coast with NDBC buoy measurements appears to suggest that the bias and the rms difference in the wave height are closely related to the bias and the rms difference in the input wind field.

The normalized bias and rms difference between the WAM output and altimeter measurement in the Yellow and East China Seas are shown in Fig. 11. The wind speed range in the Yellow and East China Seas comparison is considerably smaller than the storm comparison in the Atlantic Ocean. The data scatter of wave height biases generally increases with the wind speed bias. The anomaly of the negative wave height bias in the region of positive wind bias as observed in the Atlantic comparison is not apparent in the Yellow and East China Seas. Also, the distribution of the wave height scatter index as a function of wind speed scatter index in the Atlantic storm data (Fig. 10(d)) is considerably tighter than those in the Yellow and East China Seas (Figs. 11(b) and 11(d)). This is because the range of wave ages in the Atlantic comparison of storm events is much narrower (0.8 to 2.8). In contrast, there are many cases of low-wind, high-swell conditions in the Yellow and East China Seas data set. The range of wave ages in the 1994 database is 0.8 to 6.9 for groundtrack 69, and 0.7 to 5.5 for groundtrack 26. For reference, the data points with different C/U_{10} range are illustrated with different plotting symbols in Figs. 10 and 11. To illustrate the wave age effect, we have presented the data for $C/U_{10} < 2$ in Figs. 11(a) and 11(b), and the data for $C/U_{10} > 2$ in Figs. 11(c) and 11(d). The correlation of the normalized bias or rms difference with wave age is obviously much better in the group of young wave ages (compare Figs. 11(a) and 11(b) with 11(c) and 11(d)). The fraction of outliers in cases of large C/U_{10} (Figs. 11(c) and 11(d)) is also much higher than the corresponding fraction in cases of small C/U_{10} (Figs. 11(a) and 11(b)).

From this limited comparison, it is found that for cases with active wind generation (small values of C/U_{10}), the normalized bias and rms difference in wave heights are closely correlated to the corresponding statistics in the wind field. Furthermore, the magnitudes of the normalized bias and rms difference in the wave field are comparable to those in the wind field. For cases with large wave ages, say

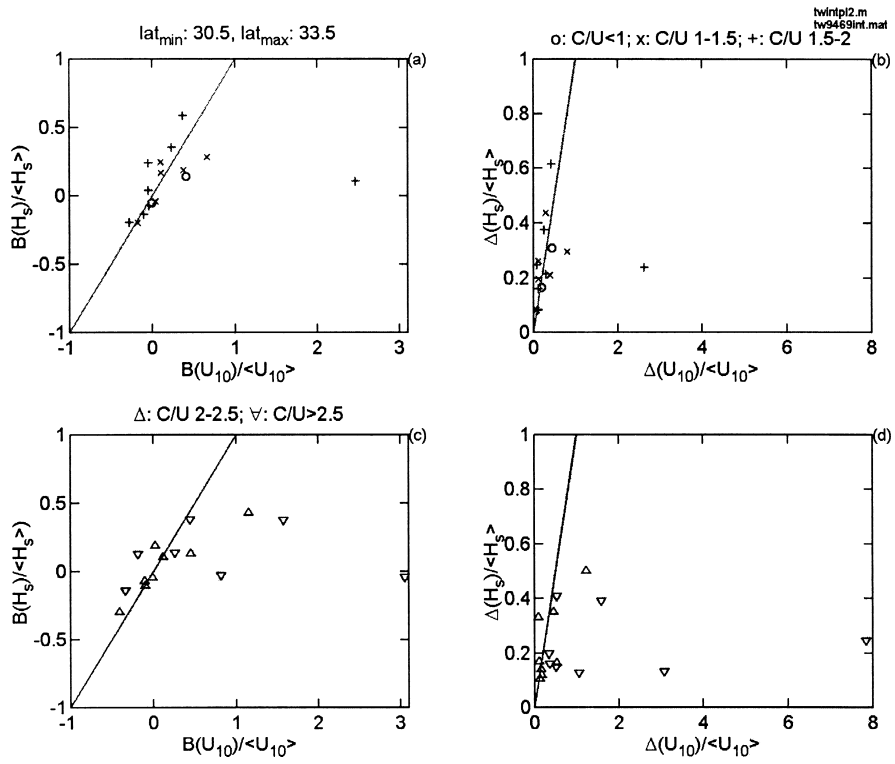

Fig. 11. Scatter plots showing the correlation of (a), (c) normalized bias, and (b), (d) rms difference of wave heights with respect to the corresponding quantities of the wind speeds. Plotting symbols for different wave ages are the same as those in Fig. 10. Data with wave ages less than 2 are plotted in the top row (a), (b), and those with larger wave ages are plotted in the bottom row (c), (d).

$C/U_{10} > 2.5$, there is little dependence of the wave height bias or scatter index on the corresponding statistics of the wind speeds. Outliers or data points deviating from the correlation curve in the population of small C/U_{10} are considerably smaller than those in the population of large C/U_{10}.

Interestingly, the magnitudes of the normalized bias and rms difference in the wave field under large wave ages are similar to those under young wave ages even when the normalized bias and rms difference in the wind field are very large. This may suggest that ocean wave models are more robust in general as compared to atmospheric models. While extremely large deviations in wind speeds exist (normalized bias more than 3 and scatter index approaches 8), the wave model output rarely exceeds 0.6 in these two statistics (Figs. 11(c) and 11(d)).

5. Summary and Conclusions

Spaceborne measurements represent a good data source for the study of global and regional wind and wave conditions. The wind speed and wave height measured by satellite altimeters are in excellent agreement with ocean buoy measurements (e.g., Gower, 1996; Hwang *et al.*, 1998a). The spatial measurements can be used to validate the spatial distributions of winds and waves from model output. In this paper, we investigate the wind and wave distributions in the Yellow and East China Seas with the output from two groundtracks of the TOPEX altimeter. The distributions of winds and waves in the region reveal the significant effects of the Kuroshio based on a more extensive study using all 17 TOPEX groundtracks (Hwang and Teague, 1998; Hwang *et al.*, 1998b).

The spaceborne data are also used for temporal and spatial comparisons with the WAM hindcast of the region. The temporal comparison is further divided into (a) average over a region from 3 to 9 degrees latitude along a groundtrack, and (b) seasonal average along a section of the groundtrack. These average quantities from TOPEX and WAM are in good agreement in terms of mean and standard deviation (Table 1). The difference between altimeter measurements and numerical simulations is approximately 10%, with WAM overestimating most of the time. The median value of the rms differences is 0.4 m with a correlation coefficient of ~0.9 (Table 2). These figures are compared to 0.15 m and 0.97, respectively, from TOPEX and buoy comparisons in the Gulf of Mexico region for comparable spatial and temporal separations (Hwang *et al.*, 1998a). The rms difference of wind speeds in the TOPEX and WAM comparison in the Yellow and East China Seas is ~2 m/s with a correlation coefficient of ~0.83. The corresponding values from TOPEX and buoy comparisons in the Gulf of Mexico

region are 1.2 m/s and 0.9, respectively.

The comparison of spatial distributions of WAM simulations and TOPEX measurements is made with 32 cycles from each of the two groundtracks over 3- to 9-degree (latitude) segments. Figure 4 shows the cycle-by-cycle distributions along 9-degree latitude. The level of agreement between numerical simulations and altimeter measurements varies significantly from cycle to cycle. In many cases, opposite trends in the spatial distributions of wave heights and wind speeds are found. The statistics of bias, rms difference, linear regression coefficient and correlation coefficient from 32 cycles of both groundtracks are analyzed (Fig. 9 shows results of the 3-degree processing). A rather large percentage (~50%) of cases show poor agreement based on a combination of low correlations, large rms differences or biases, and regression coefficients deviate significantly from one. There are indications that the wave age is a factor affecting the performance of wave modeling skills (Figs. 10 and 11). Generally speaking, the normalized bias and rms difference in the wave field are correlated closely to those of the wind field under the condition of active wind-wave generation, such as in the winter months in the Yellow and East China Seas. The correlation in the errors statistics of wave to those of winds decreases in cases of large wave age.

Comparisons presented here indicate that the numerical wave simulation skills are good in the projection of average quantities, such as the mean wave height for a give location, but relatively poor for the coherence structure, such as the spatial distribution of the wave field. The measurements from remote sensing devices, including spaceborne and airborne, are of spatial sampling in nature. These measurements represent a good data source to enhance our understanding of the spatial properties of the wind and wave fields. The spaceborne data are especially useful for studying regional wind and wave climates. The spatial resolution of spaceborne altimeters (7 km alongtrack) is considerably higher than typical in situ measurements for such applications.

Acknowledgements

This research is sponsored by the Office of Naval Research, and the U.S. Army Corps of Engineers. The WAM hindcast was conducted as a part of the Military RDT&E Program of the U.S. Army Engineer Waterways Experiment Station's Coastal and Hydraulics Laboratory. Permission was granted by Headquarters, U.S. Army Corps of Engineers, to publish this information. (NRL contribution JA/7332-98-0002).

Appendix. The WAM Model and NCEP Wind Fields

The WAM model (WAMDI Group, 1988) is a third generation spectral wave model which incorporates the physics of wave evolution and propagation without ad hoc assumptions concerning the spectral shape or limit to wave growth. The evolution of the directional wave spectrum is determined through the integration of the spectral wave transport equation given by:

$$\frac{\partial F}{\partial t} + (\cos\phi)^{-1}\frac{\partial}{\partial \phi}\left(c_\phi \cos\phi F\right) + \frac{\partial}{\partial \lambda}\left(c_\lambda F\right) + \frac{\partial}{\partial \theta}\left(c_\theta F\right) = S \qquad \text{(A1)}$$

where

$$S = S_{\text{in}} + S_{\text{ds}} + S_{\text{nl}} + S_{\text{bot}} \qquad \text{(A2)}$$

and $F(f, \theta, \phi, \lambda, t)$ is the two-dimensional wave energy spectrum and is a function of frequency f, direction θ, and time t, in a spherical coordinate system with ϕ representing latitude and λ representing longitude. The component propagation velocities are given by c_ϕ, c_λ, and c_θ. The source/sink term S includes the wind input S_{in}, nonlinear wave-wave interaction S_{nl}, the wave dissipation S_{ds} and an optional bottom dissipation term for shallow water S_{bot}. The model version used in this study is cycle 4. The wind input source term S_{in} for this version is described by Janssen (1991). In Janssen's method wave growth rate is calculated as a function of the sea surface roughness as well as the wind. S_{in} is a quadratic function of the friction velocity, u^* which is related to the roughness and roughness is related to the wave height or sea state. This coupling of the winds and waves enhances young wind sea growth over older wind sea growth. The wave dissipation S_{ds} due to whitecapping is based on Hasselmann (1974), Komen *et al*. (1984), and Janssen (1991). This term removes energy from the high frequency region due to wave breaking and is proportional to f^4. The nonlinear energy transfer S_{nl} is represented by the discrete interaction approximation (DIA), described in Hasselmann *et al*. (1985) and WAMDI Group (1988), of the full Boltzman-integral (Hasselmann and Hasselmann, 1985).

The WAM model provides an option for running in a shallow water mode. For this the deep-water transport equation must be modified to include depth dependent effects such as refraction, shoaling, and energy loss due to bottom friction. The source function is extended to include the bottom friction term S_{bot} taken from the Joint North Sea Wave Project (JONSWAP) study (Hasselmann *et al*., 1973) and given by:

$$S_{\text{bot}} = -\frac{\Gamma}{g^2}\frac{\omega^2}{\sinh^2 kD}F \qquad \text{(A3)}$$

where Γ = constant = 0.038 $m^2 s^{-3}$. This bottom friction term may require tuning for other geographical areas (WAMDI

Group, 1988), however, this was not done for the present study. In addition modifications are made to other terms in the transport equation to account for the depth dependence of the finite depth dispersion relation. The infinite depth group velocity for propagation is replaced by the appropriate expression for finite depth and the phase velocity in the wind input term is replaced by the appropriate value for finite depth. Based on Hasselmann and Hasselmann (1981), the nonlinear transfer for finite depth is the same as for infinite depth except for a scaling factor. The great circle refraction term, represented by c_θ, is extended to include refraction due to changes in water depth. Current refraction is also an option in the model but was not used in this study. The numerical scheme for propagation is a first order upstream difference in time and space while the source terms are integrated using a second order implicit scheme.

Several studies have made comparisons of WAM results to measured data in deep water. Cardone *et al*. (1995) compared WAM results using global scale analysis wind fields from the ECMWF, FNMOC, and UKMO forecasting centers to that using wind fields derived from manual kinematic analysis. This comparison showed that the error in the forecast centers' wind fields masked any errors due to deficiencies in the WAM model. The scatter index (SI, ratio of rms difference to mean of the measurement) in the model time series SWH at each buoy varied from 10% to 14%, or about half of the SI found with the forecast centers' wind fields. Cardone *et al*. (1996) have shown the WAM model performs well for wave conditions up to 12 m during moderate to extreme storm events. However Tolman (1992), Lin and Huang (1996) and Bender (1996) show that the WAM implementation of the first order propagation scheme is highly dissipative causing excessive attenuation in swell propagation over large distances and have proposed higher order schemes to reduce this numerical error. The wave hindcast setup used in the present comparison study consisted of a global 1° Lat/Lon grid to generate input wave boundary conditions, and a regional 0.25° Lat/Lon grid including the Yellow Sea, East China Sea, and the Sea of Japan which ranged from 25°N to 51°N latitude and 115°E to 145°E longitude.

The wind input for the global and regional WAM hindcast was a global wind product produced by the National Centers for Environmental Prediction (NCEP, formerly the National Meteorological Center). Two types of global forecast products are generated on a daily basis at NCEP. The aviation (3-day) forecast and the 10-day medium-range forecasts (MRF). The MRF product was used in this study in a hindcast mode so that only the analysis wind fields are used. Initial conditions for the MRF are provided by the NCEP Global Data Assimilation System (GDAS) (Kanamitsu, 1989) which is a four dimensional analysis/forecast system. A six hour forecast from the MRF model is used as a first guess to the next analysis. The initial conditions for the global model are provided by an optimal interpolation scheme using observations and the first guess. The model used for the global analysis (GDAS), the aviation forecast, and the medium-range forecasts is the MRF model (Sela, 1980, 1988). The model has undergone continuous changes since it became operational in 1985. The 1988 version is fully documented in NMC Development Division (1988). The version used to produce the wind fields in this study is that used in the daily production during 1994 (Kistler, 1998, personal communication). The following provides a brief description of this version.

The MRF model is spectral in the horizontal domain and has a horizontal triangular truncation of T126. For calculation of nonlinear quantities and physics a transformation to a Gaussian grid is made which is equivalent to roughly a 1° grid. The vertical domain is represented by 28 unequally spaced sigma levels. The model has a comprehensive set of physical parameterizations (Kalnay *et al*., 1990) which include convective heating, large scale precipitation and evaporation of falling rain. The boundary layer physics is based on the Monin-Obukhov similarity theory.

In an effort to predict the forecast skill NCEP has been using ensemble forecasting operationally since December 1992 (Kalnay and Toth, 1996). Wobus and Kalnay (1995) presented a method using regional anomalies of circulation and ensemble forecasts consisting of forecasts from the United Kingdom Meteorological Office (UKMO), the Japan Meteorological Agency (JMA), and the European Centre for Medium-Range Weather Forecasting (ECMWF). Although the NCEP forecasts show considerable skill in general, Wobus and Kalnay found that, during an example case in 1993, the forecast of the regional circulation was very poor in an area including Japan and Korea.

The NCEP winds, which are provided at approximately 0.94° Lat/Lon resolution, were bilinearly interpolated to a 1° resolution for the global hindcast and a 0.25° resolution for the regional hindcast. The global hindcast was run with a temporal resolution of 6 hours, which is the resolution provided by NCEP. The NCEP winds were linearly interpolated to a 3 hour resolution for the regional hindcast. One of the standard WAM output files includes the significant wave height (SWH), H_s, friction velocity u^*, and drag coefficient C_D at every grid point. The model wind speed at a 10 m elevation is given by $U_{10} = u^* C_D^{-1/2}$. The wave height, wave direction, wave period (peak and average), wind speed and wind direction of the model outputs are extracted along TOPEX tracks for comparison.

References

Bauer, E. and C. Staabs (1998): Statistical properties of global significant wave heights and their use for validation. *J. Geophys. Res.*, **103**, 1153–1166.

Bauer, E., S. Hasselmann and K. Hasselmann (1992): Validation and assimilation of Seasat altimeter wave heights using the WAM wave model. *J. Geophys. Res.*, **97**, 12671–12682.

Bender, L. C. (1996): Modification of the physics and numerics in a third-generation ocean wave model. *J. Atmos. Ocean. Tech*., **13**, 726–750.

Bratos, S. M. (1997): Comparison between third generation and second generation ocean wave models. M.S. Thesis, Texas A&M University, College Station.

Brown, G. S., H. R. Stanley and N. A. Roy (1981): The wind speed measurement capability of spaceborne radar altimeters. *IEEE J. Oceanic Eng*., **OE-6**, 59–63.

Cardone, V. J. (1992): On the structure of the marine surface wind field. p. 54–66. In *The 3rd International Workshop of Wave Hindcasting and Forecasting*, Montreal, Quebec, May 19–22.

Cardone, V. J., H. C. Grabber, R. E. Jensen, S. Hasselmann and M. J. Caruso (1995): In search of the true surface wind field in SWADE IOP-1: ocean wave modeling perspective. *The Global Atmos. and Ocean Sys*., **3**, 107–150.

Cardone, V. J., R. E. Jensen, D. T. Resio, V. R. Swail and A. T. Cox (1996): Evaluation of contemporary ocean wave models in rare extreme events: "Halloween Storm" of October, 1991; "Storm of the Century" of March, 1993. *J. Atmos. Ocean. Tech*., **13**, 198–230.

Chelton, D. B. and F. J. Wentz (1986): Further development of an improved altimeter wind speed algorithm. *J. Geophys. Res*., **91**, 14250–14260.

Chuang, W. S. and W. D. Liang (1994): Seasonal variability of intrusion of the Kuroshio water across the continental shelf northeast of Taiwan. *J. Oceanogr*., **50**, 531–542.

Ebuchi, N. and H. Kawamura (1994): Validation of wind speeds and significant wave heights observed by the TOPEX altimeter around Japan. *J. Oceanogr*., **50**, 479–487.

Freilich, M. H. and P. G. Challenor (1994): A new approach for determining fully empirical altimeter wind speed model functions. *J. Geophys. Res*., **99**, 25051–25062.

Gower, J. F. R. (1996): Intercomparison of wave and wind data from TOPEX/POSEIDON. *J. Geophys. Res*., **101**, 3817–3829.

Hasselmann, K. (1974): On the spectral dissipation of ocean waves due to whitecapping. *Boundary Layer Meteorol*., **6**, 107–127.

Hasselmann, K., T. P. Barnett, E. Bouws, H. Carlson, D. E. Cartwright, K. Enke, J. A. Ewing, D. E. Hasselmann, P. Kruseman, A. Meerburg, P. Muller, K. J. Olbers, K. Richter, W. Sell and W. H. Walden (1973): Measurements of wind-wave growth and swell decay during the Joint North Sea Wave Project (JONSWAP). *Dtsch. Hydrogr. Z*., **A8**(12), 95 pp.

Hasselmann, S. and K. Hasselmann (1981): A symetrical method computing the nonlinear transfer in a gravity-wave spectrum. *Hamb. Geophys. Einzelschriften, Reihe A: Wiss. Abhand*., **52**, 138 pp.

Hasselmann, S. and K. Hasselmann (1985): Computations and parameterizations of the nonlinear energy transfer in a gravity wave spectrum, 1, A new method for efficient computations of the exact nonlinear transfer integral. *J. Phys. Oceanogr*., **15**, 1369–1377.

Hasselmann, S., K. Hasselmann, J. H. Allender and T. P. Barnett (1985): Computations and parameterizations of nonlinear energy transfer in a gravity wave spectrum, 2, Parameterizations of the nonlinear energy transfer for application in wave models. *J. Phys. Oceanogr*., **15**, 1378–1391.

Hsueh, Y. (1988): Recent current observations in the Eastern Yellow Sea. *J. Geophys. Res*., **93**, 6875–6884.

Hsueh, Y., C.-S. Chern and J. Wang (1993): Blocking of the Kuroshio by the continental shelf northeast of Taiwan. *J. Geophys. Res*., **98**, 12351–12359.

Hwang, P. A. and W. J. Teague (1998): Technical evaluation of constructing wind and wave climatologies using spaceborne altimeter output, with a demonstration study in the Yellow and East China Seas. Naval Research Laboratory Memo. Rep. NRL/MR/7332-98-8216, 41 pp.

Hwang, P. A., W. J. Teague, G. A. Jacobs and D. W. Wang (1998a): A statistical comparison of wind speed, wave height and wave period derived from satellite altimeters and ocean buoys in the Gulf of Mexico region. *J. Geophys. Res*., **103**, 10451–10468.

Hwang, P. A., W. J. Teague, G. A. Jacobs and D. W. Wang (1998b): Wind and waves in the Yellow and East China Seas from satellite altimeter measurement. *Pacific Ocean Remote Sensing Conference*, **1**, 321–325.

Janssen, P. A. E. M. (1991): Quasi-linear theory of wind wave generation applied to wave forecasting. *J. Phys. Oceanogr*., **21**, 745–754.

Janssen, P. A. E. M., P. Lionello, M. Reistad and A. Hollingsworth (1989): Hindcasts and data assimilation studies with the WAM model during the Seasat period. *J. Geophys. Res*., **94**, 973–993.

Kalnay, E. and Z. Toth (1996): Ensemble prediction at NCEP. *Preprints, 11th AMS Conference on Numerical Weather Prediction*, Norfolk Virginia.

Kalnay, E., M. Kanamitsu and W. E. Baker (1990): Global numerical weather prediction at the National Meteorological Center. *Bull. Amer. Meteor. Soc*., **71**, 1410–1428.

Kanamitsu, M. (1989): Description of the NMC global data assimilation and forecast system. *Wea. and Forecasting*, **4**, 335–342.

Komen, G. J., S. Hasselmann and K. Hasselmann (1984): On the existence of a fully developed windsea spectrum. *J. Phys. Oceanogr*., **14**, 1271–1285.

Lie, H. J. and C. H. Cho (1994): On the origin of the Tsushima Warm Current. *J. Geophys. Res*., **99**, 25081–25091.

Lin, R. Q. and N. E. Huang (1996): The Goddard coastal wave model. Part I: Numerical method. *J. Phys. Oceanogr*., **26**, 833–847.

Lionello, P., H. Gunther and P. A. E. M. Janssen (1992): Assimilation of altimeter data in a global third-generation wave model. *J. Geophys. Res*., **97**, 14453–14474.

NMC Development Division Staff (1988): Documentation of the research version of the Medium Range Forecast model. NMC Documentation Series #1.

NOAA (1986): ETOPO 5 digital relief of the surface of the earth. Data Announcement 86-MGG-07, 2 pp. (available from National Geophysical Data Center, Washington, D.C., 20233).

Romeiser, R. (1993): Global validation of the wave model WAM over a one-year period using Geosat wave height data. *J. Geophys. Res*., **98**, 4713–4726.

Sela, J. (1980): Spectral Modeling at the National Meteorological Center. *Mon. Wea. Rev*., **108**, 1279–1292.

Sela, J. (1988): The new T80 NMC operational spectral model. p. 312–313. *Preprints 8th Conference on Numerical Weather Prediction*, Baltimore, American Meteorological Society, Maryland, Boston.

Smith, W. H. F. and P. Wessel (1990): Gridding with continuous curvature splines in tension. *Geophysics*, **55**, 293–305.

Sterl, A., G. J. Komen and P. D. Cotton (1998): Fifteen years of global wave hindcasts using winds from the European Centre for Medium-Range Weather Forecasts reanalysis: Validating the reanalyzed winds and assessing the wave climate. *J. Geophys. Res*., **103**, 5477–5492.

Tolman, H. L. (1992): Effects of numerics on the physics in a third-generation wind-wave model. *J. Phys. Oceanogr*., **22**, 1095–1111.

WAMDI Group (1988): The WAM model—a third generation wave prediction model. *J. Phys. Oceanogr*., **18**, 1775–1810.

Wang, Y. and D. G. Aubrey (1987): The characteristics of China coastline. *Cont. Shelf Res*., **7**, 329–349.

Wessel, P. and W. H. F. Smith (1991): Free software helps map and display data. *EOS Trans. Amer. Geophys. U*., **72**, 441, 445–446.

Witter, D. L. and D. B. Chelton (1991): A Geosat altimeter wind speed algorithm and a method for altimeter wind speed algorithm development. *J. Geophys. Res*., **96**, 8853–8860.

Wobus, R. L. and E. Kalnay (1995): Three years of operational prediction of forecast skill at NMC. *Mon. Wea. Rev*., **123**, 2132–2148.

Wu, J. (1992): Near-nadir microwave specular returns from the sea surface-altimeter algorithm for wind and wind stress. *J. Atm. Oceanic Tech*., **9**, 659–667.